

# Iron, Nitrogen Co-Doped Carbon Spheres as Low Cost, Scalable Electrocatalysts for the Oxygen Reduction Reaction

Jingyu Feng, Rongsheng Cai, Emanuele Magliocca, Hui Luo, Luke Higgins, Giulio L. Fumagalli Romario, Xiaoqiang Liang, Angus Pedersen, Zhen Xu, Zhenyu Guo, Arun Periasamy, Dan Brett, Thomas S. Miller, Sarah J. Haigh, Bhoopesh Mishra, and Maria-Magdalena Titirici\*

Atomically dispersed transition metal-nitrogen-carbon catalysts are emerging as low-cost electrocatalysts for the oxygen reduction reaction in fuel cells. However, a cost-effective and scalable synthesis strategy for these catalysts is still required, as well as a greater understanding of their mechanisms. Herein, iron, nitrogen co-doped carbon spheres (Fe@NCS) have been prepared via hydrothermal carbonization and high-temperature post carbonization. It is determined that FeN<sub>4</sub> is the main form of iron existing in the obtained Fe@NCS. Two different precursors containing Fe<sup>2+</sup> and Fe<sup>3+</sup> are compared. Both chemical and structural differences have been observed in catalysts starting from Fe<sup>2+</sup> and Fe<sup>3+</sup> precursors. Fe<sup>2+</sup>@NCS-A (starting with Fe<sup>2+</sup> precursor) shows better catalytic activity for the oxygen reduction reaction. This catalyst is studied in an anion exchange membrane fuel cell. The high open-circuit voltage demonstrates the potential approach for developing high-performance, low-cost fuel cell catalysts.

development is that the kinetics of the oxygen reduction reaction (ORR) occurring at the fuel cell cathode is slow, restricting energy conversion efficiencies.<sup>[2]</sup> Pt-based catalysts perform best and are the materials that have been widely applied commercially. However, they suffer from scarcity and high cost while further stability improvements are also required.<sup>[3]</sup> To achieve widespread and sustainable commercialization of fuel cells, the key goals are increasing their durability and decreasing their cost (US DOE 2025 targets: 5000 h lifetime and \$ 40/kW<sub>net</sub> at 500 000 systems per year).<sup>[4]</sup>

Great progress has been made to date in designing non-precious metal-based catalysts for fuel cells, including developing Fe, Co, Mn based catalysts to have activities

comparable to the noble-metal catalysts.<sup>[2,5]</sup> The M-N-C catalysts (where M is a transition metal) are among the most promising electrocatalysts.<sup>[6]</sup> The key characteristic of these catalysts is the presence of M-N<sub>x</sub> which has shown high stability and high catalytic activity.<sup>[7]</sup> Of these materials, Fe-N-C catalysts have shown

## 1. Introduction

Hydrogen and fuel cells play a key role toward reaching 2050 net-zero carbon emissions targets for generating CO<sub>2</sub> free electricity and transportation.<sup>[1]</sup> A key challenge in their

J. Feng, H. Luo, G. L. F. Romario, X. Liang, Z. Xu, Z. Guo, M.-M. Titirici  
Department of Chemical Engineering  
Imperial College London  
South Kensington Campus, London SW7 2AZ, UK  
E-mail: m.titirici@imperial.ac.uk  
R. Cai, S. J. Haigh  
Department of Materials  
University of Manchester  
Manchester M13 9PL, UK

 The ORCID identification number(s) for the author(s) of this article can be found under <https://doi.org/10.1002/adfm.202102974>.

© 2021 The Authors. Advanced Functional Materials published by Wiley-VCH GmbH. This is an open access article under the terms of the Creative Commons Attribution License, which permits use, distribution and reproduction in any medium, provided the original work is properly cited.

DOI: 10.1002/adfm.202102974

E. Magliocca, D. Brett, T. S. Miller  
Electrochemical Innovation Lab  
Department of Chemical Engineering  
University College London  
Torrington Place, London WC1E 7JE, UK  
L. Higgins, B. Mishra  
School of Chemical and Process Engineering  
University of Leeds  
Leeds LS2 9JT, UK  
X. Liang  
School of Environmental and Chemical Engineering  
Xi'an Polytechnic University  
Xi'an 710048, P. R. China  
A. Pedersen  
Department of Materials  
Imperial College London  
South Kensington Campus, London SW7 2AZ, UK  
A. Periasamy  
Department of Chemistry  
University of Surrey  
Surrey GU2 1XH, UK

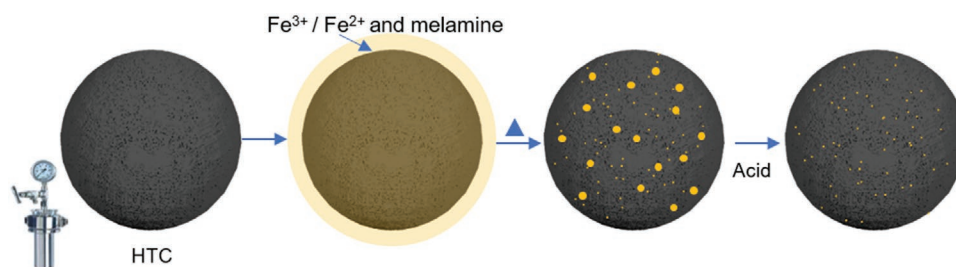


**Figure 1.** Schematic illustration for the synthesis of Fe@NCS-A.

superior performance, which has attracted considerable recent attention from the research community.<sup>[8]</sup> Various aspects, including the local structure of the Fe-N sites, synergistic performance of different iron species, stability of the Fe-N coordination structures, active site evolution from raw precursors into the final carbon materials during carbonization, and the ORR pathways have been investigated.<sup>[9]</sup> Although great progress has been made, there are still challenges in establishing the exact structure-to-property correlation in such catalysts, which is essential for the rational design and synthesis of new catalysts with tailored activities for wide ranges electrocatalytic processes.<sup>[7]</sup>

Also, looking for a cost-effective and scalable way to synthesize effective catalysts and supports is necessary to support commercial uptake of the technology.<sup>[10]</sup> Hydrothermal carbonization (HTC) converts biomass or biomass-derived precursors into oxygenated hydrothermal carbons, which can yield advantageous stable and conductive porous structures as well as superior catalytic activity by additional carbonization or hybridization with active transitional metal and nitrogen sources.<sup>[11]</sup>

Herein, a facile route to construct scalable, low-cost iron nitrogen-doped carbon spheres (Fe@NCS) as high-performance ORR catalysts is presented. The primary synthetic strategy is illustrated in **Figure 1**. First, hydrothermal carbon spheres (CS) with abundant oxygen functionalities were prepared by HTC of xylose.<sup>[12]</sup> The obtained hydrothermal CS were then impregnated with iron precursors ( $\text{FeCl}_2$  or  $\text{FeCl}_3$ ) and a nitrogen precursor (melamine), followed by two-step carbonization under inert  $\text{N}_2$  gas (see Supporting Information).<sup>[8a]</sup> During the carbonization process, iron and nitrogen were hybridized into the carbon support, thus forming Fe@NCS. Fe@NCS powder was treated with 0.1 M HCl to remove any free metallic iron species formed on the surface, allowing only Fe-N<sub>x</sub> complexes to remain (Fe@NCS-A, where A represents acid). Samples that are impregnated with  $\text{FeCl}_2$  or  $\text{FeCl}_3$  are denoted as  $\text{Fe}^{2+}$ @NCS-A and  $\text{Fe}^{3+}$ @NCS-A, respectively, where -A refers to acid wash. 1.8 g of Fe@NCS catalyst ( $\approx 51\%$  yield) can be easily obtained in a one-batch, demonstrating the scalability of this reaction (Figure S1, Supporting Information). For comparison, CS and NCS were also prepared.

## 2. Results and Discussion

Scanning electron microscopy (SEM) images in Figure S2, Supporting Information show that all samples present a well-defined spherical morphology, with diameters around 300–500 nm. Compared to the smooth surface of CS and NCS,  $\text{Fe}^{2+}$ @NCS-A displays a much rougher surface, likely due to the

Fe assisting the graphitization of amorphous carbon.<sup>[13]</sup> A few smaller high-brightness nanoparticles (NPs) can also be seen in the SEM images of the Fe@NCS samples (Figure S2c,d, Supporting Information), which are mostly removed by the HCl wash (Figure S2e,f, Supporting Information). To further analyze the materials, high-resolution high-angle annular dark-field scanning transmission electron microscopy (HAADF-STEM) was employed.

The overview of the morphology of the  $\text{Fe}^{2+}$ @NCS-A and  $\text{Fe}^{3+}$ @NCS-A was shown in HAADF-STEM images (**Figure 2a,b**). The CS in both  $\text{Fe}^{2+}$ @NCS-A and  $\text{Fe}^{3+}$ @NCS-A are in the range of 200–500 nm. After the acid wash, the surface of most CS has a uniform brightness with only a small portion of the CS showing the presence of the NPs (Figures S4a and S5a, Supporting Information). Energy-dispersive X-ray spectroscopy (EDS) was performed to map the presence of Fe species in the  $\text{Fe}^{2+}$ @NCS-A and  $\text{Fe}^{3+}$ @NCS-A samples. As can be seen in Figure 2a,b, for the CS where no NPs are visible, the Fe signal is well-distributed, suggesting that Fe may exist in the form of isolated sites. The formation of the well-distributed sites has been reported elsewhere which could be attributed to several facts, such as 1) oxygen group-rich precursors, 2) low iron content, 3) high nitrogen content, 4) high surface area carbon support, etc.<sup>[14]</sup> The aim is to protect and prevent the Fe sites from agglomerating into particles. So far, no noticeable differences in morphology could be seen in both  $\text{Fe}^{2+}$ @NCS-A and  $\text{Fe}^{3+}$ @NCS-A.

To get a complete picture of the obtained catalysts, the CS showing the presence of the NPs were also investigated. EDS was conducted (Figures S4c and S5c, Supporting Information), one could see the associated particles mainly consisted of Fe. From the high-resolution HAADF STEM images and their fast Fourier transform (FFT) images (Figures S4d–f and S5d–f, Supporting Information), it could be observed that the size of the associated particles in both samples are in the range of 10–30 nm. For  $\text{Fe}^{2+}$ @NCS-A, interplanar spacings measured from the FFT image are around 0.20, 0.23, and 0.40 nm, which correspond to the (002), ( $\bar{1}\bar{1}2$ ) and ( $\bar{1}\bar{1}0$ ) of diffractions for  $\text{Fe}_3\text{C}$  (PDF#00-003-0989). As for  $\text{Fe}^{3+}$ @NCS-A, interplanar spacings measured from the FFT image are 0.19, 0.18, and 0.24 nm, which correspond to (0 $\bar{3}\bar{1}$ ), ( $2\bar{2}\bar{1}$ ) and (210) of reflections for  $\text{Fe}_3\text{C}$  (PDF#00-003-0989). These findings agree with the crystal structure suggested by XRD (Figure S3a,b, Supporting Information). The  $\text{Fe}_3\text{C}$  in some of the  $\text{Fe}^{2+}$ @NCS-A and  $\text{Fe}^{3+}$ @NCS-A samples might be due to the particles being embedded deep inside the CS (Figure S6, Supporting Information) and therefore inaccessible to the HCl wash.

CS with well-dispersed Fe sites are compared with CS fully loaded with Fe particles in Figure S7, Supporting Information.

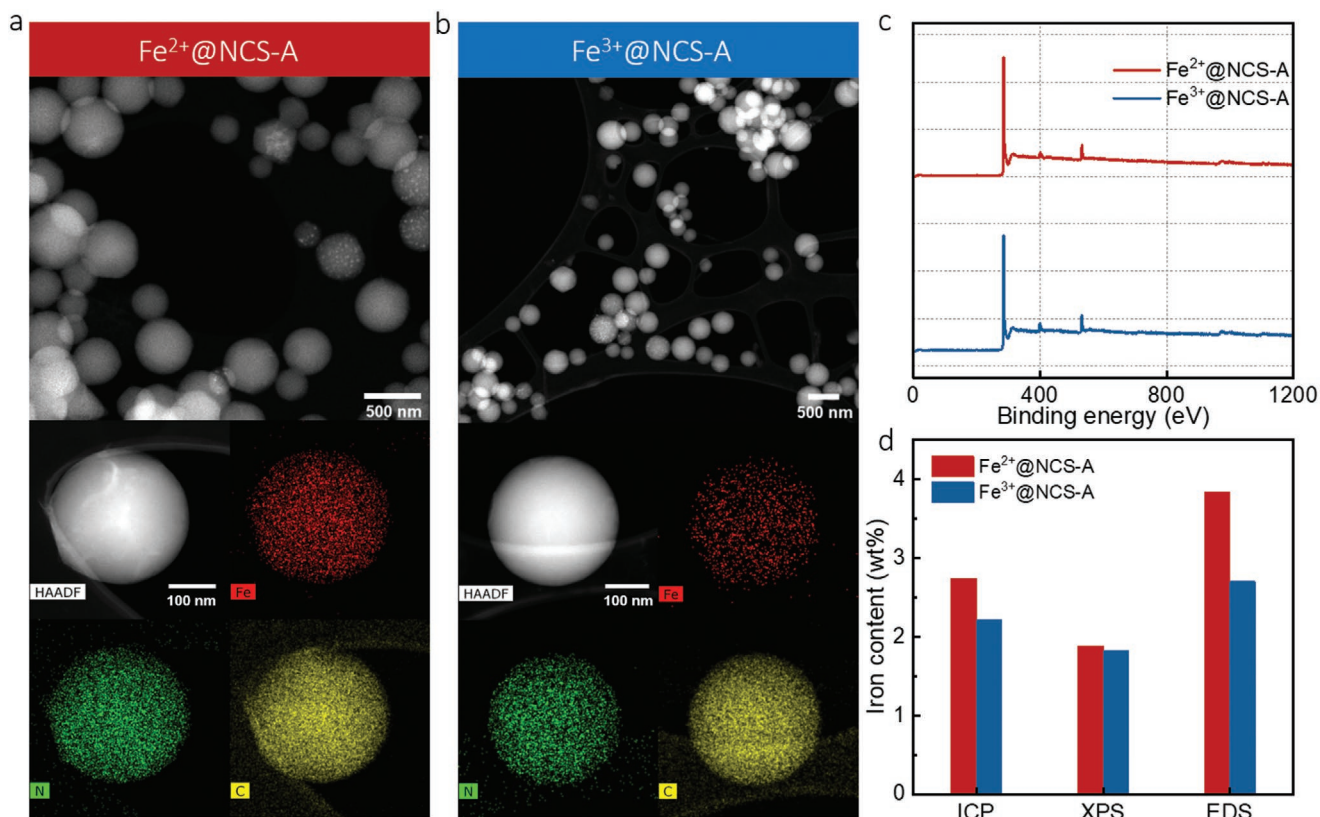


**Figure 2.** a) top HAADF-STEM image of Fe<sup>2+</sup>@NCS-A, bottom EDS mapping results of Fe<sup>2+</sup>@NCS-A, b) top HAADF-STEM image of Fe<sup>3+</sup>@NCS-A, bottom EDS mapping results of Fe<sup>3+</sup>@NCS-A, c) XPS survey of Fe<sup>2+</sup>@NCS-A and Fe<sup>3+</sup>@NCS-A, and d) the iron content of Fe<sup>2+</sup>@NCS-A and Fe<sup>3+</sup>@NCS-A from ICP-MS, XPS, and TEM-EDS.

From EDS mapping, both CS have nearly the same carbon signal intensity. The CS with only isolated Fe sites show a stronger N signal ( $\approx 6$  wt%), around three times more N signal intensity than the CS loaded with Fe NPs ( $\approx 2$  wt%). This confirms that the N content plays a significant role in preventing Fe agglomeration. This inhomogeneous dispersion of N is most likely originated during catalysts preparation steps. However, further experiments are required to reveal the mechanism.

To reveal the elemental composition of the catalysts, X-ray photoelectron spectroscopy (XPS) was performed. In Figure 2c, the XPS survey spectrum of Fe<sup>2+</sup>@NCS-A shows the chemical composition of C (84.2 wt%), N (5.77 wt%), O (8.15 wt%), and Fe (1.88 wt%) while Fe<sup>3+</sup>@NCS-A shows the chemical composition of C (82.12 wt%), N (8.82 wt%), O (8.82 wt%) and Fe (1.82 wt%). Inductively coupled plasma mass spectrometry (ICP-MS) was also used to analyze the iron content of Fe<sup>2+</sup>@NCS-A and Fe<sup>3+</sup>@NCS-A. With XPS surveys and TEM-EDS (Figure 2d), iron content in Fe<sup>2+</sup>@NCS-A is higher than that in Fe<sup>3+</sup>@NCS-A. Fe<sup>2+</sup>@NCS showed 2.74 wt%, 1.88 wt%, and 3.84 wt% of iron content from ICP-MS, XPS, and TEM-EDS, respectively, while Fe<sup>3+</sup>@NCS-A showed 2.22 wt%, 1.82 wt%, and 2.7 wt%, respectively. As ICP-MS is a bulk elemental analysis and XPS is more focused on the surface of catalysts, this suggests both Fe<sup>2+</sup>@NCS-A and Fe<sup>3+</sup>@NCS-A have similar Fe sites on the surface while Fe<sup>2+</sup>@NCS-A has more Fe in bulk.

To gain insights about the local structure of the Fe sites in Fe<sup>2+</sup>@NCS-A, Fe<sup>3+</sup>@NCS-A, as well as to confirm that Fe exists

in atomic form, element-selective X-ray adsorption spectroscopy (XAS) experiments were conducted at the Fe K-edge. The magnitude of the extended X-ray absorption fine structure (EXAFS) Fourier Transforms (FTs) of Fe<sup>2+</sup>@NCS-A and Fe<sup>3+</sup>@NCS-A are displayed in Figure 3a. The magnitude of the FT has a strong single peak centered around 1.6 Å (phase uncorrected) for both Fe<sup>2+</sup>@NCS-A and Fe<sup>3+</sup>@NCS-A, distinct from those of the Fe<sub>2</sub>O<sub>3</sub>, and metallic Fe references, but similar to the reference iron phthalocyanine (FePc), which has well-defined Fe-N<sub>4</sub> coordinated sites. This result confirmed the absence of Fe-oxides and metallic Fe. Further, Fe EXAFS suggests the formation of Fe-N sites.

Wavelet transform (WT) can provide both radial distance resolution and k space resolution, which is a powerful method for distinguishing the backscattering atom.<sup>[15]</sup> As shown in Figure 3b, WT analysis of Fe<sup>2+</sup>@NCS-A and Fe<sup>3+</sup>@NCS-A both show only one intensity maximum at  $\approx 4.2$  Å<sup>-1</sup>, which is very close to that in the reference FePc ( $\approx 4.2$  Å<sup>-1</sup>), but distinct from the feature of Fe<sub>2</sub>O<sub>3</sub> ( $\approx 7$  Å<sup>-1</sup>). Therefore, the EXAFS and STEM data converge to the conclusion that the majority of the Fe species in Fe<sup>2+</sup>@NCS-A, Fe<sup>3+</sup>@NCS-A are Fe-N single sites, with a tiny amount of Fe<sub>3</sub>C embedded in the CS where they are inaccessible to the HCl wash.

As up to several different Fe-N<sub>x</sub> structures have been reported and each of them can result in different catalytic performance, it is essential to determine local structure of the Fe-N<sub>x</sub> structures.<sup>[9]</sup> Building optimized structure and simulating the X-ray

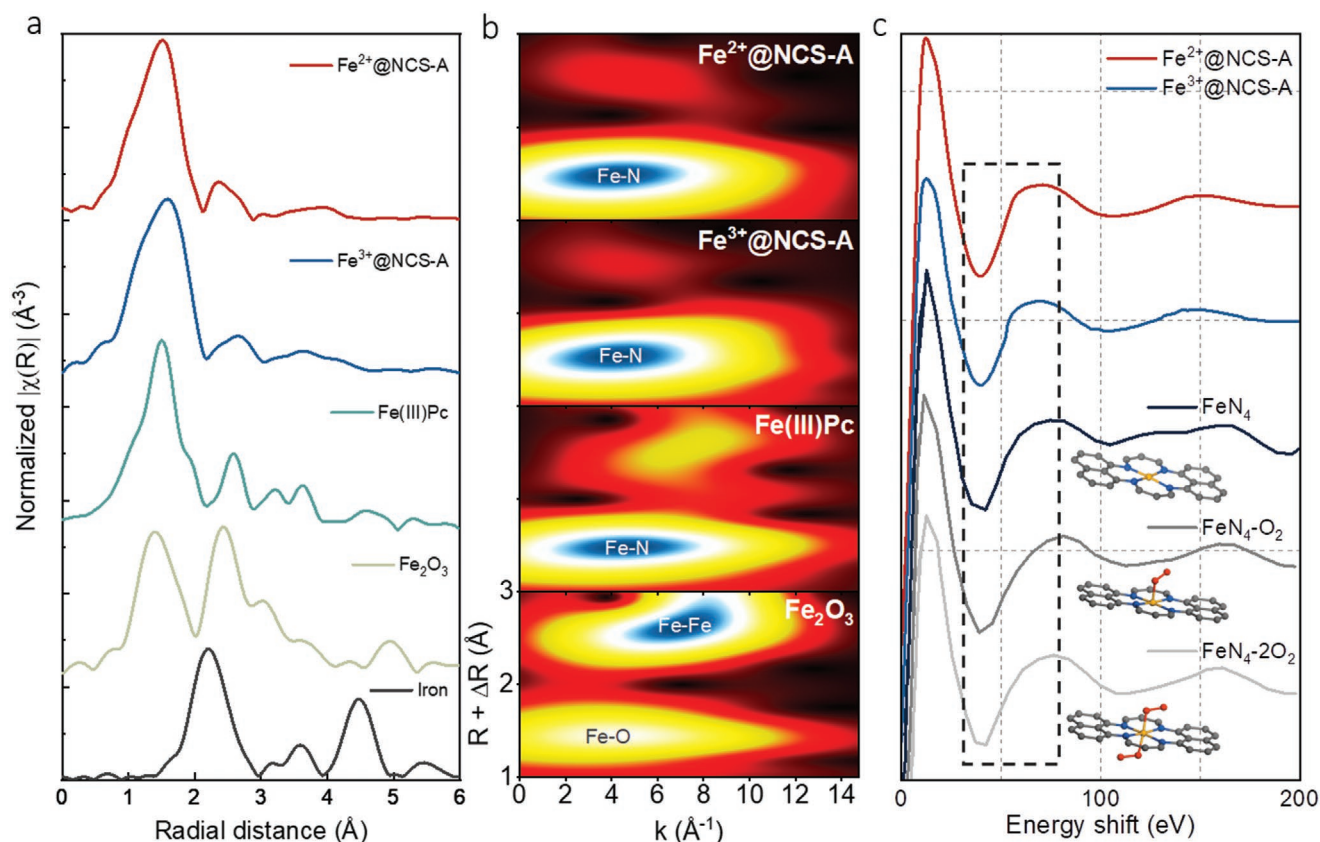


**Figure 3.** a) Fourier transform of Fe K-edge EXAFS spectra, b) wavelet transform of the  $k^2$  weighted EXAFS data of  $\text{Fe}^{2+}$ @NCS-A,  $\text{Fe}^{3+}$ @NCS-A, Fe(III) Pc, and  $\text{Fe}_2\text{O}_3$ , c) comparison between the K-edge XANES experimental spectrum of  $\text{Fe}^{2+}$ @NCS-A, and  $\text{Fe}^{3+}$ @NCS-A to the theoretical spectra  $\text{FeN}_4$ ,  $\text{FeN}_4\text{-O}_2$ ,  $\text{FeN}_4\text{-2O}_2$ . The theoretical XANES spectra are reproduced with permission.<sup>[16]</sup> Copyright 2015, Springer. (Insert: theoretical Fe-N structures where red spheres are oxygen, yellow spheres are iron, grey spheres are carbon, and blue spheres are nitrogen).

absorption near edge structure (XANES) signal via density functional theory (DFT) calculations has become a powerful way to reveal the local structure of the single Fe sites.<sup>[7,16,17]</sup> Herein, reported theoretical XANES spectra were used to compare with  $\text{Fe}^{2+}$ @NCS-A and  $\text{Fe}^{3+}$ @NCS-A experimental data (Figure 3c).<sup>[16]</sup> Only three possible matched structures  $\text{FeN}_4$ ,  $\text{FeN}_4\text{-O}_2$ ,  $\text{FeN}_4\text{-2O}_2$  represent  $\text{FeN}_4$  without oxygen ligand, with one oxygen ligand, or with two oxygen ligands attached on the center Fe, respectively. By comparing these three different structures,  $\text{FeN}_4$  without ligand attached on the Fe is the best one matched structure for both  $\text{Fe}^{2+}$ @NCS-A and  $\text{Fe}^{3+}$ @NCS-A.

To shed light on chemical configuration of Fe-N single sites, FT EXAFS fittings were performed for  $\text{Fe}^{2+}$ @NCS-A,  $\text{Fe}^{3+}$ @NCS-A using iFEFFIT (Figure 4a,b,d,e; Figures S8 and S9, Supporting Information).<sup>[18]</sup> All fittings are in good consistency with experimental data. The best fit values (Table S1, Supporting Information) for EXAFS modeling of  $\text{Fe}^{2+}$ @NCS-A give an average coordination number of  $4.0 \pm 0.4$  for Fe-N at  $2.10 \pm 0.01 \text{ \AA}$  and  $2.4 \pm 0.4$  Fe-C at  $1.92 \pm 0.01 \text{ \AA}$ . Meanwhile, the average coordination numbers for  $\text{Fe}^{3+}$ @NCS-A are  $3.4 \pm 0.1$  Fe-N at  $2.08 \pm 0.01 \text{ \AA}$  and  $1.2 \pm 0.3$  Fe-C at  $1.90 \pm 0.01 \text{ \AA}$ . In addition,  $0.5 \pm 0.1$  Fe-Fe was required for fitting  $\text{Fe}^{3+}$ @NCS-A.<sup>[5d,19]</sup> The Fe-C signal is expected due to the presence of  $\text{Fe}_3\text{C}$  in these samples, as confirmed by STEM and EDS analyses. The

absence of Fe-Fe signal in  $\text{Fe}^{2+}$ @NCS could be either due to minimal  $\text{Fe}_3\text{C}$  content or a much smaller average particle size of  $\text{Fe}_3\text{C}$ . Therefore, we propose that the iron existed primarily as  $\text{Fe-N}_x$  on the carbon substrate for both  $\text{Fe}^{2+}$ @NCS-A and  $\text{Fe}^{3+}$ @NCS-A, with  $\text{Fe}^{2+}$ @NCS-A being a fully stoichiometric  $\text{Fe-N}_4$  species.

XPS supports the speciation of Fe obtained by EXAFS. The deconvoluted N1s spectra in Figure 4c show four types of nitrogen species for both samples, in which the peak at 399.9 eV can be assigned to  $\text{FeN}_x$  complexes (Table S2, Supporting Information).<sup>[20]</sup> Besides, deconvoluted Fe2p spectra (Figure S10a, Supporting Information) showed that Fe exists as a mixture of  $2^+$  and  $3^+$  oxidation in both  $\text{Fe}^{2+}$ @NCS-A and  $\text{Fe}^{3+}$ @NCS-A with more  $\text{Fe}^{2+}$  state in  $\text{Fe}^{2+}$ @NCS-A. Also, no noticeable presence of metallic Fe can be found in Fe2p spectra. Further, the oxidation states of the Fe in  $\text{Fe}^{2+}$ @NCS-A and  $\text{Fe}^{3+}$ @NCS-A were investigated using XANES and electron paramagnetic resonance (EPR). From the Fe K-edge XANES (Figure S10b, Supporting Information) spectra, it can be seen that the white lines of  $\text{Fe}^{2+}$ @NCS-A and  $\text{Fe}^{3+}$ @NCS-A catalysts are in between the FeO and  $\text{Fe}_2\text{O}_3$  references, indicating they have oxidation states in between  $2^+$  and  $3^+$  which more closed to  $3^+$ . However, the XANES region could be influenced by local coordination structure, it might be inaccurate to compare the oxidation state directly from XANES. Therefore, EPR was

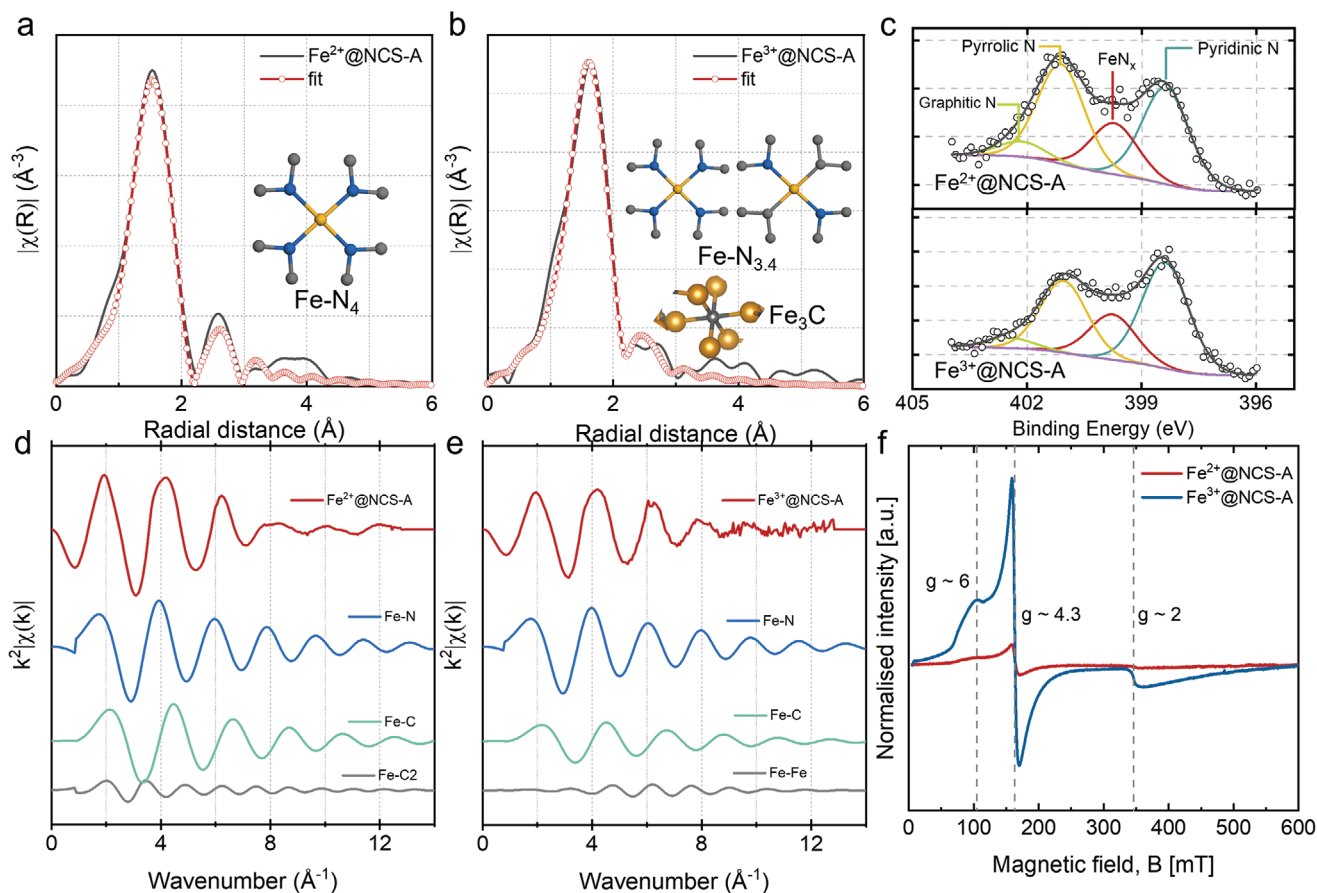


**Figure 4.** The magnitude of EXAFS FT  $k^2$ -weight Fe K-edge spectra and fitting curve of a)  $\text{Fe}^{2+}$ @NCS-A, b)  $\text{Fe}^{3+}$ @NCS-A, c) high resolution of N 1s XPS spectrum of  $\text{Fe}^{2+}$ @NCS-A and  $\text{Fe}^{3+}$ @NCS-A, d) the magnitude FT  $k^2$ -weighted Fe K-edge EXAFS spectra of  $\text{Fe}^{2+}$ @NCS-A and Fe-N, Fe-C, and Fe-C<sub>2nd</sub> paths, e) the magnitude FT  $k^2$ -weighted Fe K-edge EXAFS spectra of  $\text{Fe}^{3+}$ @NCS-A and Fe-N path, Fe-C path, and Fe-Fe path iron carbide, f) X-band EPR of  $\text{Fe}^{3+}$ @NCS-A and  $\text{Fe}^{2+}$ @NCS-A.

performed to investigate the electronic structure of  $\text{Fe}^{3+}$ @NCS-A and  $\text{Fe}^{2+}$ @NCS-A. EPR results shown in Figure 2f reveal the  $\text{Fe}^{3+}$ @NCS-A has a stronger response than  $\text{Fe}^{2+}$ @NCS-A, which suggests greater  $\text{Fe}^{3+}$  content in  $\text{Fe}^{3+}$ @NCS-A. From the EPR signals, rhombic symmetry systems with  $\text{Fe}^{3+}$  high spin ( $S = 5/2$ ) can be determined, with  $g \approx 6$  and  $g \approx 2$  assigned to  $\text{Fe}^{3+}$  with square pyramidal coordination. Meanwhile,  $g \approx 4.3$  originates from  $\text{Fe}^{3+}$  with a rhombic ligand field.<sup>[21]</sup> As stated in Figure 2d, iron content in  $\text{Fe}^{2+}$ @NCS-A is higher than that in  $\text{Fe}^{3+}$ @NCS-A. Thus the missing Fe signal in EPR suggests a higher  $\text{Fe}^{2+}$  content in the  $\text{Fe}^{2+}$ @NCS-A than  $\text{Fe}^{3+}$ @NCS-A. This difference in iron oxidation states might stem from the iron precursors that could be further responsible for a different catalytic activity.

Besides Fe active sites, it has also been reported that the structure of the carbon support, such as surface area, pore size, and graphitization contents, also plays a critical role. Therefore, to get more insights into the structural information from the obtained catalysts, wide angle X-ray scattering (WAXS), small angle X-ray scattering (SAXS), and nitrogen physical adsorption analyses were performed. Compared with NCS and CS,  $\text{Fe}^{2+}$ @NCS-A and  $\text{Fe}^{3+}$ @NCS-A show more pronounced graphitic features because the incorporation of iron can catalyze

the graphitization of the carbon substrate during carbonization (Figure S6b, Supporting Information), which favors electron transfer based on the increased conductivity. Higher graphitization could also be seen in XRD and WAXS spectrums in Figure S12, Supporting Information, where sharper and right-shifted (002) peaks are presented in  $\text{Fe}^{2+}$ @NCS-A and  $\text{Fe}^{3+}$ @NCS-A. No metallic iron peak and  $\text{Fe}_3\text{C}$  could be seen in the WAXS spectrum, suggesting the well-dispersed Fe without agglomeration. Besides, no noticeable difference could be seen from the XRD spectra of  $\text{Fe}^{2+}$ @NCS-A and  $\text{Fe}^{3+}$ @NCS-A. Furthermore, specific surfaces area of these samples was determined by using Brunauer–Emmett–Teller (BET) via  $\text{N}_2$  physical adsorption (Figure S13, Supporting Information). The  $\text{Fe}^{2+}$ @NCS-A,  $\text{Fe}^{3+}$ @NCS-A, and NCS showed a specific surface area of 70, 42, and 138  $\text{m}^2 \text{g}^{-1}$ , respectively (Figure S13c, Supporting Information). Fe doping reduced the surface area suggests that Fe species were adsorbed on the surface and encapsulated in cavities during the synthesis of Fe@NCS. Pore size distribution (Figure S13g–i, Supporting Information) shows that NCS has pores at around 1 nm, where  $\text{Fe}^{2+}$ @NCS-A has pores at 1.2 nm, and  $\text{Fe}^{3+}$ @NCS-A has pores at both 1 and 1.2 nm, which showed that more micropores (pore width smaller than 2 nm) were blocked in  $\text{Fe}^{2+}$ @NCS-A. Besides, fitted SAXS

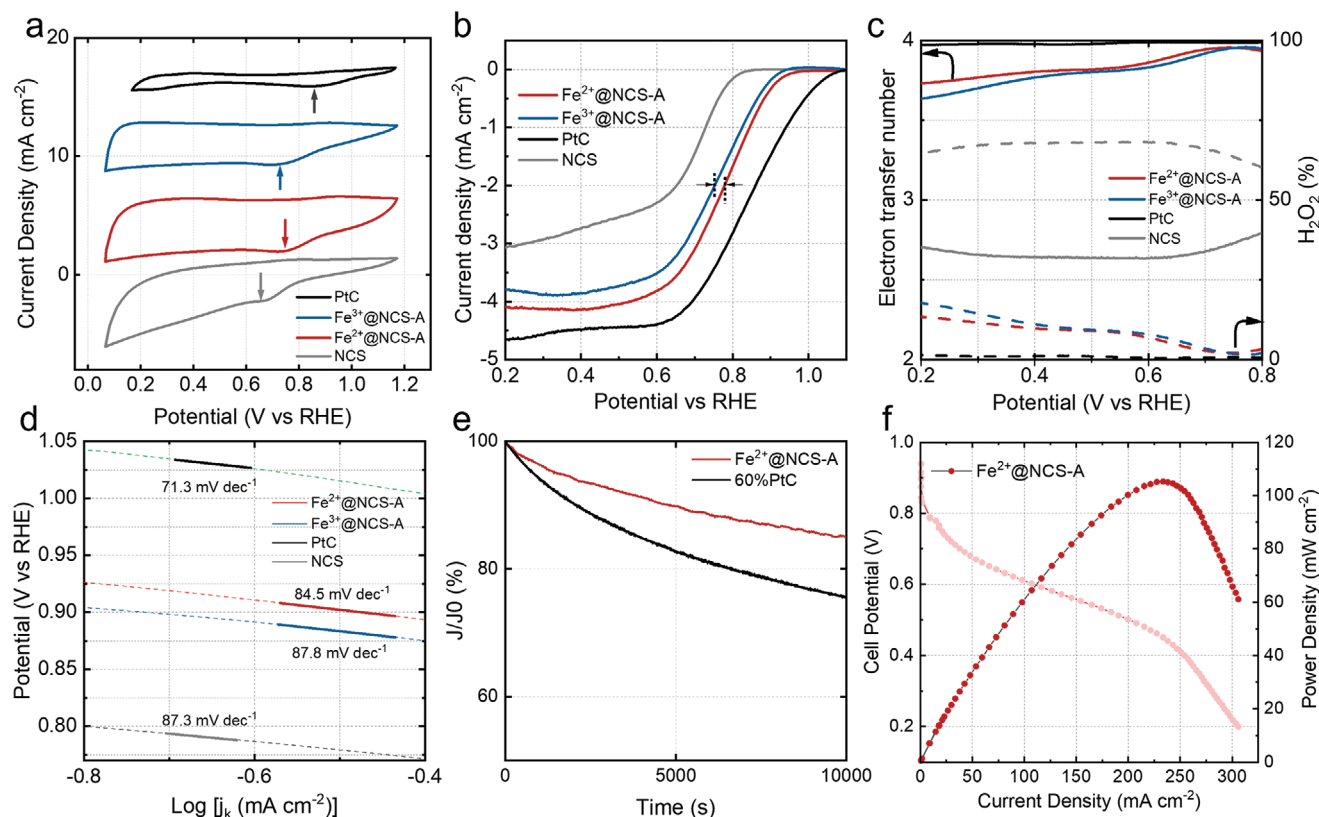


**Figure 5.** a) CV curves at 0 rpm, 100 mV s<sup>-1</sup> scan rate, b) LSV curves at 1600 rpm, 10 mV s<sup>-1</sup> scan rate, c) electron transfer number and H<sub>2</sub>O<sub>2</sub> production rate of Fe<sup>2+</sup>@NCS-A, Fe<sup>3+</sup>@NCS-A, Pt/C, and NCS, d) Tafel plots of Fe<sup>2+</sup>@NCS-A, Fe<sup>3+</sup>@NCS-A, NCS, and Pt/C, e) chronoamperometric responses of Fe<sup>2+</sup>@NCS-A and Pt/C at 0.7 V and 1600 rpm. All RDE/RRDE tests were performed in O<sub>2</sub>-saturated 0.1 M KOH, background N<sub>2</sub> current was extracted. Reference electrode: Hg/HgO, counter electrode: graphite rod. Catalyst loading: 0.28 mg cm<sup>-2</sup>, Pt loading 0.021 mg cm<sup>-2</sup>. f) AEMFC performance of Fe<sup>2+</sup>@NCS-A cathode. Polarization curve and power density plotted as a function of current density. H<sub>2</sub>-O<sub>2</sub> gases were fed at 0.3 L min<sup>-1</sup> with no back-pressurization; cathode: 2.0 mg cm<sup>-2</sup> of Fe<sup>2+</sup>@NCS-A; anode: 0.70 mg cm<sup>-2</sup> of PtRu; T<sub>cell</sub> = 60 °C (RH 100%). The membrane used in this work was low-density polyethylene-based (LDPE) anion exchange membrane and the ionomer was ETFE-benzyltrimethylammonium (BTMA) powder.

results showed the average pore diameters for Fe<sup>2+</sup>@NCS-A (1.91 nm) was smaller than Fe<sup>3+</sup>@NCS-A (2.18 nm), and NCS (2.22 nm). B values represent the relative number of pores were also fitted, and the Fe<sup>2+</sup>@NCS-A showed 510% relative number of pores compare to NCS (100%), while Fe<sup>3+</sup>@NCS-A showed 322%. This increased the relative number of pores due to the formation of closed pores which is invisible in BET. Together with BET, we could speculate that more Fe<sup>2+</sup> adsorbed into bulk and that is why smaller closed pores were generated.

To conclude, Fe<sup>2+</sup>@NCS-A has shown higher Fe<sup>2+</sup> content, fully stoichiometric Fe-N<sub>4</sub> sites, and relatively low surface area but higher surface area than Fe<sup>3+</sup>@NCS-A. These factors have shown the chemical and structural differences caused by these two precursors with different oxidation states. Further, the electrochemical characterizations were performed to investigate the catalytic performance of these catalysts.

The ORR catalytic performance of NCS, Fe<sup>2+</sup>@NCS-A, Fe<sup>3+</sup>@NCS-A, and commercial Pt/C (55–58 wt%) were evaluated by cyclic voltammetry (CV) and linear sweep voltammetry (LSV) under alkaline conditions (0.1 M KOH oxygen saturated) using a rotating disk electrode (RDE). Among all the as-prepared catalysts, the Fe<sup>2+</sup>@NCS-A shows the most promising ORR activity due to its higher amount of electroactive iron species. The CV

(Figure 5a) curves of all samples show oxygen reduction peaks (indicated by the arrows). LSV (Figure 5b) curves of Fe<sup>2+</sup>@NCS-A show an obvious peak for oxygen reduction, whose onset potential (0.94 V, the potential at -0.1 mA cm<sup>-2</sup>) is more positive than those of NCS (0.81 V), and Fe<sup>3+</sup>@NCS-A (0.91 V), 100 mV more negative than that of Pt/C (1.04 V). Fe<sup>2+</sup>@NCS-A also displays a half-wave potential of 0.79 V, which is 30 mV more positive than Fe<sup>3+</sup>@NCS-A (0.76 V), suggesting a better catalytic activity in Fe<sup>2+</sup>@NCS-A. (Figure 5b). The limiting current density of Fe<sup>2+</sup>@NCS-A is higher than Fe<sup>3+</sup>@NCS-A, suggesting more 4 electron pathway occurs in Fe<sup>2+</sup>@NCS-A. As illustrated in Figure 5d, Fe<sup>2+</sup>@NCS-A presents a Tafel slope value of 84.5 mV dec<sup>-1</sup>, slightly lower than Fe<sup>3+</sup>@NCS-A (87.8 mV dec<sup>-1</sup>), and NCS (87.3 mV dec<sup>-1</sup>). Rotating ring disk electrode (RRDE) tests show an electron transfer number from 3.7 to 3.95 for both Fe<sup>2+</sup>@NCS-A and Fe<sup>3+</sup>@NCS-A. The decreasing trend of electron transfer number suggests the 2-electron process increases at lower potentials. H<sub>2</sub>O<sub>2</sub> production showed an increasing trend from high potential to low potential (from 2–18%).

Thus, the higher onset potential, higher half-wave potential, smaller Tafel slope value, and higher electron transfer number of Fe<sup>2+</sup>@NCS-A are likely to originate from the different local coordination environments and the oxidation states of the Fe

site as Fe<sup>2+</sup>@NCS-A has a higher amount of Fe-N<sub>4</sub> sites and higher overall iron content in Fe<sup>2+</sup>. However, more experiments are needed to reveal the detailed mechanism of whether and how Fe oxidation state influences the electrocatalysis steps. It should be mentioned here that the Fe<sub>3</sub>C content in the two samples is minimal and embedded inside the CS structure, as demonstrated by our STEM, EXAFS, XPS, and WAXS data. Thus, the contribution from Fe<sub>3</sub>C toward the ORR performance should be negligible.<sup>[22]</sup>

Chronoamperometry testing was performed to check the stability of Fe<sup>2+</sup>@NCS-A. After 10 000 s at 0.7 V, due to the Fe-N single sites, nearly 85% of the current was retained for Fe<sup>2+</sup>@NCS-A, whilst Pt/C only showed 76% current retention (Figure 5e). To investigate the active site change, ex situ XPS was performed before and after the CV cycling (Figure S10c, Supporting Information). No noticeable changes in the peak shape and the decreased peak intensity might be caused by the sample peeled off during the CV cycling, resulting in a lower intensity than the one before CV cycling. To further explore the performance of Fe<sup>2+</sup>@NCS-A in real operating devices, the electrochemical performance in anion exchange membrane fuel cells (AEMFCs) was also tested.<sup>[23]</sup> The operating AEMFCs were fed with H<sub>2</sub> and O<sub>2</sub> gases. The Fe<sup>2+</sup>@NCS-catalyst was able to achieve high open-circuit potentials at 0.96 V in the operating AEMFC compared to other comparable M-N-C catalysts (Table S4, Supporting Information). Although it is still lower than Pt-based catalysts tested under similar conditions, it shows great potential after further electrode optimization.<sup>[24]</sup> The current density and power density demonstrating the promising approach for developing low-cost AEMFCs.

### 3. Conclusion

In summary, Fe, N co-doped carbon sphere electrocatalysts (Fe@NCS-A) were synthesized via a facile, green, and scalable method. The majority of Fe species were found to exist in Fe-N<sub>4</sub> sites, with a minimal amount aggregated into Fe<sub>3</sub>C NPs and embedded inside the CS structure. The optimized Fe-N<sub>4</sub> sites have been successfully obtained by starting with different Fe precursors, with Fe<sup>2+</sup>@NCS-A showing a better ORR and AEMFC activity and durability. For the formation mechanism of Fe-N<sub>4</sub> sites, we propose that the N content is key for preventing Fe aggregation. At the same time, the starting precursor and carbonization conditions are essential for determining the final configuration of the Fe-N<sub>4</sub> sites. We have proved that iron precursors with different oxidation states can lead to variants in iron species, iron sites' coordination numbers, and oxidation states in the final product, consequently influencing the final catalytic performance. However, future efforts are needed to unveil the interactions of dopants and carbon support during the carbonization process and correlate these structural features with their electrocatalytic activity. Considering the relatively low surface area of these catalysts, the next step could improve the surface area to unlock the full catalytic potential. This work addresses factors when considering the oxidation state's influence of precursors in the design of the electrocatalyst. It provides a new perspective on understanding the catalytic active sites.

### 4. Experimental Section

**Reagents and Solutions:** All chemicals were used without further purifications. D-(+)-Xylose (≥99%, 150.13 g mol<sup>-1</sup>, Sigma Aldrich), iron(II) chloride tetrahydrate (99.99%, 198.81 g mol<sup>-1</sup>, Sigma Aldrich), iron(III) chloride hexahydrate (≥99%, 270.30 g mol<sup>-1</sup>, Sigma Aldrich), melamine (99%, Sigma Aldrich), absolute ethanol (≥99.9%, Fisher Scientific), deionized water (18.2 MΩ cm), nitric acid (70%, Sigma Aldrich), and hydrochloric acid (37% ACS reagent, Sigma Aldrich).

**Synthesis of HTC CS:** Xylose, a readily available monosaccharide was used as eco-friendly precursor and the source of carbon framework for doping metal atoms. The HTC of this five-carbon sugar yielded monodispersed spherical particles with an average diameter of 320 nm (Figure S1, Supporting Information). For each of the samples, 7 g of solid xylose was dissolved in 70 mL DI water in glass beakers which were then placed in a sonication bath for 5 min and stirred for 2 h. The next stage of the synthesis was HTC of the xylose solution, whereby xylose solutions were transferred to a 100 mL hydrothermal reactor (Kemi, Anhui, China), with the reactor then placed in a pressurized furnace (Memmert, Germany) at 200 °C for 12 h. The obtained sample was further filter-washed with 500 mL water, and the inhomogeneous impurities were removed. After that, the obtained brownish powder (hydro-char) was further washed with centrifugation (Thermo Scientific, Heraeus Multifuge X1R, USA) for 10 min at 12 000 rpm. The recovered hydro-char was vacuum dried at 105 °C for 24 h to remove any remaining moisture, producing completely dry samples fit for milling. Milling was carried out by using a pestle and mortar, to yield a fine powder of hydrothermal CS.

**Synthesis of NCS:** Melamine was chosen as the nitrogen precursor due to its rich N content, and wide availability. 500 mg melamine was first dissolved in 50 mL of absolute EtOH via bath sonication for 10 min. Then, 500 mg of obtained brownish CS powder was added into the melamine solution and stirred for 2 h at 300 rpm. The final solution was then rotatory dried (Scilogex RE100-S, USA) at 55 °C, and then moved to an 80 °C vacuum oven for an additional 12 h. The obtained sample was milled using a pestle and mortar for 15 min to achieve a fine powder. The carbonization was then carried out in a tubular furnace (Carbolite S.T.F., UK) by a two-step process under N<sub>2</sub> atmosphere (gas flow rate: 0.5 L min<sup>-1</sup>); first, the furnace was heated at 600 °C for 2 h with a heating rate of 5 °C min<sup>-1</sup> and then the temperature was ramped up again to 900 °C for another 2 h with a heating rate of 5 °C min<sup>-1</sup>.

**Synthesis of Iron, Nitrogen Co-Doped Nanospheres (Fe<sup>2+</sup>@NCS, and Fe<sup>3+</sup>@NCS):** To obtain Fe<sup>2+</sup>@NCS, 39.73 mg iron(II) chloride tetrahydrate (0.2 mol Fe) or 56.44 mg iron(III) chloride hexahydrate (0.208 mol Fe) was first dissolved into 50 mL of absolute EtOH via bath sonication for 10 min. The same synthesis process for the NCS was then carried out as presented above. The obtained samples were denoted as Fe<sup>2+</sup>@NCS, and Fe<sup>3+</sup>@NCS, where Fe<sup>2+</sup>/Fe<sup>3+</sup> represents the precursor's oxidation state.

**Synthesis of Fe<sup>2+</sup>@NCS-A, Fe<sup>3+</sup>@NCS-A:** The obtained Fe@NCS catalysts were further treated with 1 M HCl for 12 h at room temperature at 250 rpm on an agitation platform to remove free metal ions and the unwanted impurities. Then, the resulting solutions containing Fe@NCS were centrifuged for 10 min at 12 000 rpm to separate the catalyst from the acid. The wet catalyst was then vacuum dried at 105 °C for 12 h. The obtained samples were denoted as Fe<sup>2+</sup>@NCS-A, and Fe<sup>3+</sup>@NCS-A, where A represents the HCl acid treatment. The chemical reactions involved in this process are shown in Equations (1,2):



**Characterization:** SEM was conducted on Zeiss Leo Gemini 1525. High resolution transmission electron microscopy was conducted on all the electrode samples at an operating voltage of 300 kV. The samples were dispersed in ethanol and sonicated for 10 min, followed by casting onto lacey carbon mesh copper grids (Agar Scientific, Lacey carbon film 400 Cu). The grids were then placed in a vacuum desiccator to assist the

evaporation of the solvent overnight before loading onto the TEM sample holder. The HAADF STEM imaging and EDS elemental mapping were performed using a Thermo Fisher Titan STEM (G2 80-200) equipped with a Cs probe corrector (CEOS), a ChemiSTEM Super-X E.D.X. detector, and a HAADF detector operating with an inner angle of 55 mrad at 200 kV. The incident electron beam convergence angle was 21 mrad. The diffraction patterns of obtained Fe@NCS samples were measured with a powder X-ray diffractometer (XRD PANalytical's X'PERTPRO) in the two theta range from 10° to 85° at 3° min<sup>-1</sup>. XPS analysis was performed using a Thermo Scientific Nexsa XPS system. ICP-MS was conducted by A Nu Instruments Nu Plasma multiple collector inductively coupled plasma mass spectrometer. Before analyzing, the carbon samples were carefully weighed and digested by aqua regia using a MARS 6 microwave at 1500 W for 20 min. The solutions were further filtered and diluted with 2% HNO<sub>3</sub> and 1% HCl to achieve a concentration of Fe < 500 ppb. For each sample, two duplicates were prepared for accuracy. Nitrogen sorption isotherms were conducted at -196 °C in Micromeritics 3Flex system. The BET surface area was deduced from an analysis of the isotherm in the relative pressure range of 0.0002–0.03. The total pore volume was calculated from the amount of nitrogen adsorbed at a relative pressure of 0.99. The pore size distribution was calculated by HS-2D-NLDFT\_Carbon\_N2\_77 method using adsorption and desorption parts of the isothermal data.

**SAXS and WAXS Samples Preparation and Analysis:** Powder samples were loaded on to samples holder and the samples test was performed in beamline I22 (SM27900), Diamond Light Source, UK. Beam energy was 12.4 keV with a wavelength of 1 Å. The SAXS sample-detector distance was 5719.2 mm, and the WAXS sample-detector distance was 166.32 mm. Data was collected as a stack of 100 × 0.1 s frames and averaged. A Porod method proposed by Stevens and Dahn<sup>[25]</sup> was employed to SAXS data to probe the pore size of the carbon samples. The equation proposed by Stevens and Dahn is as follows.

$$I(q) = \frac{A}{q^a} + \frac{B_1 a_1^4}{(1 + a_1^2 q^2)^2} + D \quad (3)$$

where  $I(q)$  is the scattered intensity as a function of  $q$ ,  $A$  is a scale factor for the surface scattering at low  $q$ ,  $B_1$  is a scale factor for the pore scattering, which is proportional to the total surface area of pores.  $D$  is a constant background, and  $a_1$  is the characteristic length and associated with the radius of a spherical pore, by  $R = a_1 \times \sqrt{10}$ . This equation can be modified so that  $B_2$  becomes proportional to the number of pores by adding an  $a_1^2$  term.

$$I(q) = \frac{A}{q^a} + \frac{B_2 a_1^6}{(1 + a_1^2 q^2)^2} + D \quad (4)$$

**X-Ray Absorption Spectroscopy Sample Preparation and Analysis:** To obtain a good XAS signal, 15–20 mg samples (85–90 wt%) were well mixed with 1.5–3 mg (10–15 wt%) cellulose and pressed into 5 mm pellet with a thickness of 0.5–1 mm, 5 microliters of DI water was added into the mixture before pelleting to maintain the pellet structure. XAS measurements were performed at beamline B18 of Diamond Light Source in transmission and fluorescence mode using Stern–Heald geometry using ion-chambers. Transmission mode data were used due to their superior quality. The data were normalized to the incoming incident energy and processed with the Athena software. An  $E_0$  value of 7112.0 eV was used to calibrate all data with respect to the first inflection point of the absorption K-edge of an Fe foil. EXAFS curve fitting was performed with Artemis. Fe-N<sub>4</sub>-C structure was built, and geometry optimized using Dmol3. The optimized structures were calculated through FEFF 8 to obtain the paths. The EXAFS spectra were obtained by subtracting pre-edge and post-edge background from the overall absorption and then normalizing with respect to the edge step. Subsequently, the  $\chi(k)$  data of 3.0 to 10 Å<sup>-1</sup> was used for Fourier transformed to real R space using a Hanning window ( $dk = 1.0 \text{ Å}^{-1}$ ) to separate the EXAFS contributions from different coordination shells. To obtain the quantitative structural parameters around central atoms,

least-squares curve parameter fitting was performed using the ARTEMIS module of IFEFFIT software packages. Addition of a shell in EXAFS modeling was justified by a significant lowering of the reduced chi-square value.  $S_0^2 = 0.85 \pm 0.03$  was obtained by fixing the coordination number of powdered Fe standards to their known crystallographic structure.

**EPR:** EPR measurements were performed at Imperial College London. ≈40 mg of sample was filled into a capillary with an inner diameter of 3 mm Wilmad quartz (CFQ) EPR tubes (Sigma Aldrich) that were weighed before and after filling to determine the precise mass of each sample. Continuous-wave (CW) EPR spectra were recorded on an X-band CW ELEXSYS E500 EPR spectrometer (Bruker, Germany) equipped with a cryogen-free variable temperature cryostat (Oxford Instruments, Oxfordshire, UK). EPR spectra were recorded at ≈ 9.7 GHz under non-saturating Fe(III) conditions, corresponding to an incident microwave power of 2 mW (at 5 K). A magnetic field frequency of 100 kHz, modulation amplitude of 1 G, power attenuation 20 dB, and receiver gain 75 dB were used with the external magnetic field sweeping in 1190 steps from 5 to 600 mT. For non-lorentzian lines observed in the EPR spectra here (Figure 4f) one should use the turning point to evaluate the effective  $g$  values.

**Electrochemical Tests:** Inks containing the different catalysts were prepared for a RDE testing to evaluate their performance for the catalysis of ORR. 8 mg of catalyst powder was weighed and mixed with 1400 μL of deionized (DI) water, 528 μL of EtOH, and 72 μL of 5 wt% NafionD-521 dispersion in water and 1-propanol (Alfa Aesar). The Nafion dispersion was used as a binder for the components of the ink. The inks were then placed in a bath sonicator for 10 min before undergoing ultrasonic liquid processing in a probe sonicator (Fisherbrand model 705, USA) for 10 min per sample, under a 5 s on and 5 s off regime. The working electrodes were then prepared by pipetting 14 μL of the inks onto a polished glassy carbon electrode of diameter 5 mm, resulting in a catalyst loading of 0.28 mg cm<sup>-2</sup>. The catalyst modified electrodes were left rotating at 700 rpm for 1 h to dry under room temperature before electrochemical testing. A commercial 60 wt% Pt/C (JM HiSPEC 9100) working electrode was prepared in the same way; using 1 mg of Pt/C instead of 8 mg, which resulted in a Pt loading of 0.021 mg cm<sup>-2</sup>. Electrochemical tests were conducted in alkaline (50 mL 0.1 M KOH, 99.995% suprapur) conditions for comparison purposes in a three-electrode system, with the continuous bubbling of oxygen (N5.8) through the electrolytes. The electrochemical data was gathered at room temperature and ambient pressure on a RDE system using an AUTOLAB PGSTAT 101 and a MULTI AUTOLAB M101 (CH Instruments). The configuration included a three-electrode system formed of a glassy carbon 5 mm diameter RDE working electrode, a graphite rod as the counter electrode, and the Hg/HgO as the reference electrode. CV curves were acquired by cycling the potential after purging O<sub>2</sub> for 30 min. Linear sweep voltammograms (LSV) were acquired at an electrode rotation speed of 1600 rpm with a scan rate of 10 mV s<sup>-1</sup> in an O<sub>2</sub>-saturated solution unless stated otherwise. The potentials have been converted to reversible hydrogen electrode by following a calibration method reported.<sup>[26]</sup>

**Gas Diffusion Electrodes Fabrication and AEMFC Testing:** For the anode gas diffusion electrode (GDE), a PtRu/C (Alfa Aesar, Johnson Matthey HiSpec 12100, 50 wt% Pt and 25 wt% Ru) catalyst and the ETFE-g-poly (VBTMAC) ionomer powder (IEC = 1.24 ± 0.06 mmol g<sup>-1</sup>), 20 wt% of the total solid mass, were mixed together using H<sub>2</sub>O: IPA (1:1) as solvent. This catalyst ink was homogenized with ultrasound for 30 min, then sprayed onto a Freudenberg H23C8 carbon paper gas diffusion substrate with a microporous layer using an ultrasonic automated coated system (ExactoCoat, Sono-Tek). For the cathode G.D.E., Fe<sup>2+</sup>@NCS-A was used as a catalyst instead. The geometric surface areas of all GDEs were 5.0 cm<sup>2</sup>, the loading for the anode was 0.70 mg<sub>PtRu</sub> cm<sup>-2</sup> and 2.0 mg<sub>cat</sub> cm<sup>-2</sup> for the cathode. The Anion Exchange Membrane (AEM) used in this work was a radiation-grafted low-density polyethylene (LDPE) film (25 μm, IEC = 2.87 ± 0.05 mmol g<sup>-1</sup>) with covalently-bound cationic headgroups.<sup>[23,27]</sup> Both the anode, cathode GDEs and membrane were hydrated in DI water for 20 min and then soaked two times in aqueous 1.0 M KOH to remove impurities and ion exchange the quaternary ammonium hydroxide groups before cell assembly. AEMFCs

with 5 cm<sup>2</sup> active area were assembled in single-cell hardware with a single channel serpentine flow field, using 4.5 N m torque (5 cm<sup>2</sup> fuel cell fixture supplied by Scribner, USA). The pitch was kept around 25% of the total GDE thickness using Teflon gaskets. No prior hot-pressing of the membrane electrode assembly (MEA) was used. An 850e fuel cell test station (Scribner Associates, USA) was used for testing. The fuel cell temperature was controlled at 60 °C. H<sub>2</sub> and O<sub>2</sub> gas feeds were supplied to the anode and cathode, respectively, with flow rates of 0.3 L min<sup>-1</sup> (SLPM) with no back-pressurization (RH = 100%). The MEA was activated by discharging the cell at a constant voltage of 0.5 V during cell heating, with retention of this cell voltage until a steady current density was observed. Beginning-of-life AEMFC performance data were collected under controlled galvanostatic discharge steps where data (at each current density) was only recorded once the potentials had stabilized. The internal ohmic resistance was estimated using the 850e instrument's internal current interrupt method.

## Supporting Information

Supporting Information is available from the Wiley Online Library or from the author.

## Acknowledgements

The authors thank Giannantonio Cibin and Nitya Raman from the B18 (SP26201) and Andy Smith from the I22 beamlines (SM27900) at Diamond Light Source to support and assist the measurements. T.S.M. thanks the EPSRC for support via EP/P023851/1 and EP/S01800X/1. J.Y.F., Z.X., and Z.Y.G. thank the support from Chinese Scholarship Council. R.C. and S.J.H. thank EPSRC EP/P009050/1. The authors want to thank Prof. John Varcoc's group for providing the membrane and the ionomer.

## Conflict of Interest

The authors declare no conflict of interest.

## Data Availability Statement

The data that support the findings of this study are available on request from the corresponding author. The data are not publicly available due to privacy or ethical restrictions.

## Keywords

anion exchange membrane fuel cells, electrocatalysts, non-PGM catalysts, oxygen reduction reaction, xylose

Received: March 27, 2021

Revised: July 22, 2021

Published online: August 16, 2021

[1] Committee on Climate Change, **2019**, Reducing UK emissions - 2019 progress report to parliament. This report is laid before Parliament on July 2019 and is available online at: [www.theccc.org.uk/publications](http://www.theccc.org.uk/publications).

[2] M. Lefèvre, E. Proietti, F. Jaouen, J.-P. Dodelet, *Science* **2009**, 324, 71.

[3] C. Cui, L. Gan, M. Heggen, S. Rudi, P. Strasser, *Nat. Mater.* **2013**, 12, 765.

- [4] a) S. T. Thompson, B. D. James, J. M. Huya-Kouadio, C. Houchins, D. A. DeSantis, R. Ahluwalia, A. R. Wilson, G. Kleen, D. Papageorgopoulos, *J. Power Sources* **2018**, 399, 304; b) S. T. Thompson, D. Papageorgopoulos, *Nat. Catal.* **2019**, 2, 558.
- [5] a) A. Sarapuu, E. Kibena-Pöldsepp, M. Borghei, K. Tammeveski, *J. Mater. Chem. A* **2018**, 6, 776; b) J. Lilloja, E. Kibena-Pöldsepp, A. Sarapuu, J. C. Douglin, M. Käärik, J. Kozlova, P. Paiste, A. Kikas, J. Aruväli, J. Leis, V. Sammelselg, D. R. Dekel, K. Tammeveski, *ACS Catal.* **2021**, 11, 1920; c) R. Praats, M. Käärik, A. Kikas, V. Kisand, J. Aruväli, P. Paiste, M. Merisalu, J. Leis, V. Sammelselg, J. H. Zagal, S. Holdcroft, N. Nakashima, K. Tammeveski, *Electrochim. Acta* **2020**, 334, 135575; d) S. Ratso, N. Ranjbar Sahraie, M. T. Sougrati, M. Käärik, M. Kook, R. Saar, P. Paiste, Q. Jia, J. Leis, S. Mukerjee, F. Jaouen, K. Tammeveski, *J. Mater. Chem. A* **2018**, 6, 14663; e) R. Sibul, E. Kibena-Pöldsepp, S. Ratso, M. Kook, M. T. Sougrati, M. Käärik, M. Merisalu, J. Aruväli, P. Paiste, A. Treshchalov, J. Leis, V. Kisand, V. Sammelselg, S. Holdcroft, F. Jaouen, K. Tammeveski, *ChemElectroChem* **2020**, 7, 1739; f) S. Ratso, M. Käärik, M. Kook, P. Paiste, V. Kisand, S. Vlassov, J. Leis, K. Tammeveski, *ChemElectroChem* **2018**, 5, 1827.
- [6] a) S. Gupta, D. Tryk, I. Bae, W. Aldred, E. Yeager, *J. Appl. Electrochem.* **1989**, 19, 19; b) S. Chen, F. Bi, K. Xiang, Y. Zhang, P. Hao, M. Li, B. Zhao, X. Guo, *ACS Sustainable Chem. Eng.* **2019**, 7, 15278.
- [7] H. Fei, J. Dong, Y. Feng, C. S. Allen, C. Wan, B. Voloskiy, M. Li, Z. Zhao, Y. Wang, H. Sun, P. An, W. Chen, Z. Guo, C. Lee, D. Chen, I. Shakir, M. Liu, T. Hu, Y. Li, A. I. Kirkland, X. Duan, Y. Huang, *Nat. Catal.* **2018**, 1, 63.
- [8] a) J. Li, L. Jiao, E. Wegener, L. L. Richard, E. Liu, A. Zitolo, M. T. Sougrati, S. Mukerjee, Z. Zhao, Y. Huang, F. Yang, S. Zhong, H. Xu, A. J. Kropf, F. Jaouen, D. J. Myers, Q. Jia, *J. Am. Chem. Soc.* **2020**, 142, 1417; b) M. L. Pegis, D. J. Martin, C. F. Wise, A. C. Brezny, S. I. Johnson, L. E. Johnson, N. Kumar, S. Rauegi, J. M. Mayer, *J. Am. Chem. Soc.* **2019**, 141, 8315; c) Y. Wang, Y.-J. Tang, K. Zhou, *J. Am. Chem. Soc.* **2019**, 141, 14115; d) A. Zitolo, N. Ranjbar-Sahraie, T. Mineva, J. Li, Q. Jia, S. Stamatini, G. F. Harrington, S. M. Lyth, P. Krttil, S. Mukerjee, E. Fonda, F. Jaouen, *Nat. Commun.* **2017**, 8, 957; e) J. Tian, A. Morozan, M. T. Sougrati, M. Lefèvre, R. Chenitz, J.-P. Dodelet, D. Jones, F. Jaouen, *Angew. Chem.* **2013**, 52, 6867; f) N. R. Sahraie, U. I. Kramm, J. Steinberg, Y. Zhang, A. Thomas, T. Reier, J.-P. Paraknowitsch, P. Strasser, *Nat. Commun.* **2015**, 6, 8618.
- [9] K. Mao, L. Yang, X. Wang, Q. Wu, Z. Hu, *J. Phys. Chem. Lett.* **2020**, 11, 2896.
- [10] A. Li, S. A. Nicolae, M. Qiao, K. Preuss, P. A. Szilágyi, A. Moores, M.-M. Titirici, *ChemCatChem* **2019**, 11, 3602.
- [11] a) K. Wang, H. Wang, S. Ji, H. Feng, V. Linkov, R. Wang, *RSC Adv.* **2013**, 3, 12039; b) M.-M. Titirici, M. Antonietti, *Chem. Soc. Rev.* **2010**, 39, 103.
- [12] M.-M. Titirici, M. Antonietti, N. Baccile, *Green Chem.* **2008**, 10, 1204.
- [13] a) H. Zhong, C. Shi, J. Li, R. Yu, Q. Yu, H. Liu, Y. Yao, J. Wu, L. Zhou, L. Mai, *Chem. Commun.* **2020**, 56, 4488; b) T. Feng, M. Zhang, *Chem. Commun.* **2018**, 54, 11570; c) E. Thompson, A. E. Danks, L. Bourgeois, Z. Schnepf, *Green Chem.* **2015**, 17, 551.
- [14] L. Zhao, Y. Zhang, L.-B. Huang, X.-Z. Liu, Q.-H. Zhang, C. He, Z.-Y. Wu, L.-J. Zhang, J. Wu, W. Yang, L. Gu, J.-S. Hu, L.-J. Wan, *Nat. Commun.* **2019**, 10, 1278.
- [15] H. Funke, A. Scheinost, M. Chukalina, *Phys. Rev. B* **2005**, 71, 094110.
- [16] A. Zitolo, V. Goellner, V. Armel, M.-T. Sougrati, T. Mineva, L. Stievano, E. Fonda, F. Jaouen, *Nat. Mater.* **2015**, 14, 937.
- [17] J. Li, M. T. Sougrati, A. Zitolo, J. M. Ablett, I. C. Oğuz, T. Mineva, I. Matanovic, P. Atanassov, Y. Huang, I. Zhenyuk, A. Di Cicco, K. Kumar, L. Dubau, F. Maillard, G. Dražić, F. Jaouen, *Nat. Catal.* **2020**, 4, 10.
- [18] B. Ravel, M. Newville, *Phys. Scr.* **2005**, 2005, 1007.
- [19] S. Ratso, A. Zitolo, M. Käärik, M. Merisalu, A. Kikas, V. Kisand, M. Rahn, P. Paiste, J. Leis, V. Sammelselg, S. Holdcroft, F. Jaouen, K. Tammeveski, *Renewable Energy* **2021**, 167, 800.

- [20] a) N. D. Leonard, S. Wagner, F. Luo, J. Steinberg, W. Ju, N. Weidler, H. Wang, U. I. Kramm, P. Strasser, *ACS Catal.* **2018**, *8*, 1640; b) K. Artyushkova, B. Kiefer, B. Halevi, A. Knop-Gericke, R. Schlogl, P. Atanassov, *Chem. Commun.* **2013**, *49*, 2539; c) K. Artyushkova, A. Serov, S. Rojas-Carbonell, P. Atanassov, *J. Phys. Chem. C* **2015**, *119*, 25917; d) S. Kattel, P. Atanassov, B. Kiefer, *Phys. Chem. Chem. Phys.* **2014**, *16*, 13800.
- [21] S. Wagner, H. Auerbach, C. E. Tait, I. Martinaiou, S. C. N. Kumar, C. Kübel, I. Sergeev, H.-C. Wille, J. Behrends, J. A. Wolny, V. Schünemann, U. I. Kramm, *Angew. Chem.* **2019**, *58*, 10486.
- [22] H. Xue, T. He, J. M. Chabu, J. Liu, H. Wu, J. Zheng, M. Tan, J. Ma, R. Shen, L. Deng, Y. Zhang, *Adv. Mater. Interfaces* **2018**, *5*, 1701345.
- [23] S. D. Poynton, R. C. T. Slade, T. J. Omasta, W. E. Mustain, R. Escudero-Cid, P. Ocón, J. R. Varcoe, *J. Mater. Chem. A* **2014**, *2*, 5124.
- [24] G. A. Ferrero, K. Preuss, A. Marinovic, A. B. Jorge, N. Mansor, D. J. L. Brett, A. B. Fuertes, M. Sevilla, M.-M. Titirici, *ACS Nano* **2016**, *10*, 5922.
- [25] D. A. Stevens, J. R. Dahn, *J. Electrochem. Soc.* **2000**, *147*, 4428.
- [26] C. Wei, R. R. Rao, J. Peng, B. Huang, I. E. L. Stephens, M. Risch, Z. J. Xu, Y. Shao-Horn, *Adv. Mater.* **2019**, *31*, 1806296.
- [27] L. Wang, J. J. Brink, Y. Liu, A. M. Herring, J. Ponce-González, D. K. Whelligan, J. R. Varcoe, *Energy Environ. Sci.* **2017**, *10*, 2154.